Image restoration algorithm for terahertz FMCW radar imaging

Hu, Weidong; Xu, Zhihao; Jiang, Huanyu; Liu, Qingguo; Yao, Zhiyu; Tan, Zhen; Ligthart, Leo P.

DOI
10.1364/AO.493964

Publication date
2023

Document Version
Final published version

Published in
Applied Optics

Research Article Vol. 62, No. 20 / 10 July 2023 / Applied Optics 5399

applied optics

Image restoration algorithm for terahertz FMCW radar imaging

Weidong Hu,[1,2] Zhihao Xu,[1,*] Huanyu Jiang,[1] Qingguo Liu,[1] Zhiyu Yao,[1] Zhen Tan,[1] and Leo P. Ligthart[3]

[1]Beijing Key Laboratory of Millimeter Wave and Terahertz Technology, Beijing Institute of Technology, Beijing 100081, China
[2]Tangshan Research Institute, Beijing Institute of Technology, Hebei, 063611, China
[3]Faculty of Electrical Engineering, Delft University of Technology, Delft 2600 GA, The Netherlands
*3220205089@bit.edu.cn

Received 24 April 2023; revised 13 June 2023; accepted 13 June 2023; posted 14 June 2023; published 3 July 2023

The terahertz frequency modulation continuous-wave (THz FMCW) imaging technology has been widely used in non-destructive testing applications. However, THz FMCW real-aperture radar usually has a small depth of field and poor lateral resolution, thus restricting the high-precision imaging application. This paper proposes a 150–220 GHz FMCW Bessel beam imaging system, effectively doubling the depth of field and unifying the lateral resolution compared to the Gaussian beam quasi-optical system. Moreover, a THz image restoration algorithm based on local gradients and convolution kernel priors is proposed to eliminate further the convolution effect introduced by the Bessel beam, thereby enhancing the lateral resolution to 2 mm. It effectively improves the image under-restoration or over-restoration caused by the mismatch between the ideal and actual point spread function. The imaging results of the resolution test target and semiconductor device verify the advantages of the proposed system and algorithm.

https://doi.org/10.1364/AO.493964

1. INTRODUCTION

Recently, terahertz (THz) imaging technology has become a research hotspot due to its unique characteristics such as non-ionization, penetrability, and hydrophilicity. It plays a vital role in standoff personnel screening [1–3], radar communication [4], biomedical imaging [5,6], materials characterization [7–9], new light field control [10,11], and non-destructive testing (NDT) [12,13], etc. In particular, the THz frequency modulated continuous-wave (THz FMCW) radar has a wide range of applications owing to its high power, miniaturization, high imaging rate, and three-dimensional (3D) imaging [14–16].

The THz FMCW radar can be classified into two categories, namely, synthetic aperture and real-aperture imaging based on their respective imaging methods. Real-aperture imaging typically provides stronger detection depth and more flexible detection options compared to synthetic aperture imaging [17]. However, the THz FMCW real-aperture radar suffers from the inherent issues of limited depth of field and poor lateral resolution. These limitations are due to the trade-off between the lateral resolution and depth of field as per the definition of the Rayleigh range of the Gaussian beam. In the case of thick targets, the lateral resolution of different sections of the target may be inconsistent, making it difficult to achieve a quantitative detection. Furthermore, the real-aperture radar is limited by the antenna aperture and point spread function (PSF) [18,19], which further impairs the lateral resolution and renders the differentiation of minor defects and the precise reconstruction of the target's shape a challenging task in practical applications. Therefore, overcoming the depth of field limitation and improving the lateral resolution is of great significance for THz FMCW imaging applications.

Bessel beams with large depths of field and self-healing properties have been extensively studied since Durnin demonstrated them in 1984 [20]. However, an ideal Bessel beam cannot be generated due to the infinite energy required. Due to its simple design and fabrication, the axicon has been widely used to generate the quasi-Bessel beam with a limited depth of field. It has been applied to various THz systems such as foreign matter detection in food [21], NDT of materials [22–24], and ultra-high-speed THz wireless communication [25]. However, the thickness of the axicon increases with respect to its base angle and diameter, resulting in low conversion efficiency. In recent years, a variety of new THz diffraction elements [26–31] have been proposed to generate a high-quality Bessel beam with a longer non-diffraction range and high conversion efficiency, showing their substantial application prospects. Therefore, introducing the non-diffraction and self-recovery characteristics of the Bessel beam into the THz FMCW real-aperture radar can improve the disadvantages of the small depth of field brought by a traditional Gaussian beam.

Furthermore, there are two main approaches to improving the lateral resolution of the THz image. One is that the system operating frequency and clear aperture can be increased. However, it will inevitably lead to a decrease in penetration and an increase in system volume. The other is the image restoration algorithm, and multiple image restoration methods have been developed to overcome resolution limitations imposed by PSF and noise. The Lucy–Richardson [32,33] and Wiener algorithms [18] are two of the most frequently used methods for THz image high-resolution restoration, but are often accompanied by the amplification of noise. While utilizing only the prior information of the blurred image itself, the total variation [34] and the normalized sparsity measurement [35] blind-deconvolution methods were also used to estimate the PSF and improve the lateral resolution, but the estimation accuracy and restoration capability are limited. In recent years, thanks to the powerful end-to-end mapping and learning capabilities of convolutional neural networks, a variety of deep learning methods [36–40] have also been proposed to implement the THz image super-resolution and have achieved good restoration results. However, when the system parameters (operating frequency, quasi-optical device parameters) are changed, the network needs to be retrained. In addition, the network restoration capability does not match the degree of image degradation, which will cause under-restoration or over-restoration of the image and cannot be accurately restored to the target shape [41].

In this paper, we introduce a non-diffracting beam into the THz FMCW real-aperture radar system, significantly improving the real-aperture radar depth of field and realizing the uniformity of the lateral resolution. Moreover, a THz image restoration algorithm based on the local gradient and convolution kernel priors is proposed, dramatically enhancing the THz image lateral resolution and improving the image under-restoration or over-restoration phenomenon caused by the mismatch between the ideal and actual PSF. The proposed system and method are more suitable for the high-precision and flexible detection of thicker multilayer composite materials.

2. SYSTEM AND METHODS

A. Circuit Architecture

The electronics architecture and de-chirp schematic of our THz radar are based on a compact homodyne architecture, as shown in Fig. 1. Compared with other signal generation methods, our FMCW signal is generated by phase-locked loop (PLL), which has better phase noise and frequency linearity. Because of the poor power flatness of the FMCW signal, it is amplified after the PLL to drive the multiplier chain and output the 150–220 GHz FMCW signal. Then the reflected radio frequency signal is mixed with the local oscillator signal to produce the intermediate frequency (IF) signal that contains the target information.

Our radar transmits a continuous-wave signal whose frequency increases linearly with time:

$$S_T(t) = \exp[j2\pi(f_0 t + 1/2Kt^2)], \tag{1}$$

where f_0 is the start frequency, t is the time-varying within the duration of the modulation cycle T, and K is the sweeping

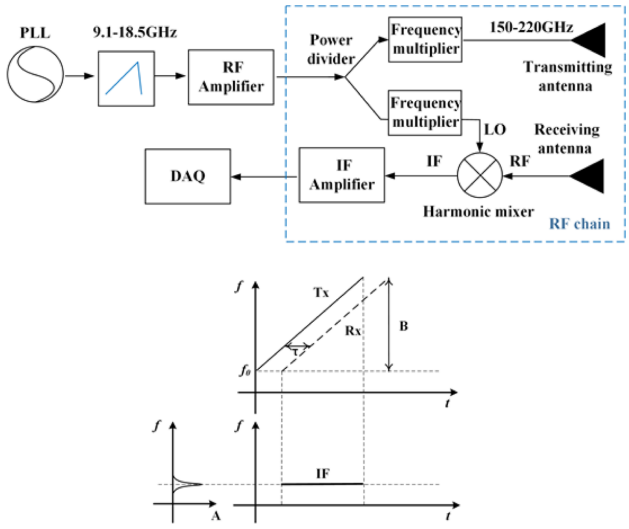

Fig. 1. Block diagram of the THz radar and de-chirp.

frequency rate which equals the ratio between the bandwidth B and T.

The echo signal reflected by the target at distance r is as follows:

$$S_{RF}(t) = \exp[j2\pi(f_0(t-\tau) + 1/2K(t-\tau)^2)], \tag{2}$$

where $\tau = 2R/c$ is the time delay of the echoes, and c is the speed of light. R is the distance between the sample under test (SUT) and the radar.

A time offset occurs between the transmitting and receiving signal caused by the delay of the transmitted signal. If the received frequencies are compared to the currently transmitted frequency by mixing, a difference frequency results that is directly proportional to the delay and to the distance between the radar and the SUT:

$$S_{ZF}(t) = \mathrm{rect}(t) \cdot \exp[j2\pi(f_0\tau + Kt\tau - 1/2K\tau^2)], \tag{3}$$

$$\mathrm{rect}(t) = \begin{cases} 1 & \tau \le t \le T \\ 0 & \text{else,} \end{cases} \tag{4}$$

where $\mathrm{rect}(t)$ is the rectangular window function. To evaluate the beat frequencies, we transformed the measured signal to the frequency domain by applying a fast Fourier transform (FFT), and the range information of the target is reflected in the frequency information of the IF signal:

$$f_{\mathrm{IF}} = K\tau = 2KR/c. \tag{5}$$

The range profile of the target can be obtained by time-frequency conversion, which is also the principle of FMCW radar thickness measurement. When the radar carries the two-dimensional (2D) scanning operation to the target, we can obtain the target's 3D imaging result.

B. Quasi-Optical System

Due to the ultra-wideband frequency response of the THz quasi-optical device, the THz real-aperture radar usually uses polyethylene lens antennas or metal mirror antennas to achieve

spatial constraints on the THz beam to further improve the lateral resolution. We use an easily fabricated axicon to convert the incident Gaussian beam into the Bessel beam, simplifying the design of the quasi-optical system. Certainly, we can also utilize novel diffraction elements to generate higher quality and a higher conversion efficiency Bessel beam. The schematic diagram for the generation of the Bessel beam by the axicon is shown in Fig. 2, and the 3D spatial intensity distribution of our system's PSF is [20]

$$\mathrm{psf}(x, y, z) = \frac{4k \sin\alpha_0}{\omega_0} \frac{z}{Z} J_0\left(k\sqrt{x^2+y^2}\sin\alpha_0\right) \exp\left(-\frac{2z^2}{Z}\right). \tag{6}$$

From formula (6), it can be seen that the phase distribution of the Bessel beam is only related to z, so it has the property of a large depth of field. x, y, z is the spatial coordinate under the Cartesian coordinate system, $k = 2\pi/\lambda$ is the angular wavenumber in free space, λ is the working center wavelength, ω_0 is the waist radius of the incident Gaussian beam, Z is the non-diffraction range, J_0 is the zero-order Bessel function, and α_0 is the semi-apex angle.

The full width at half-maximum (FWHM) of the Bessel beam is

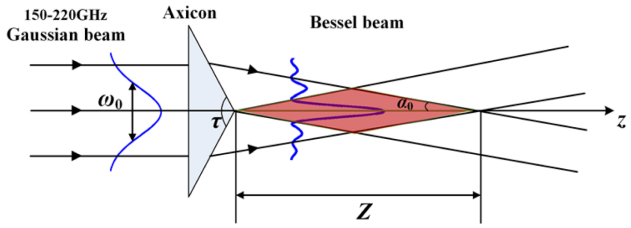

Fig. 2. Schematic diagram for the generation of the THz Bessel beam by the axicon.

$$\omega = 2.2/k\sin(\alpha_0). \tag{7}$$

According to Snell's law, the semi-apex angle α_0 can be calculated as

$$\alpha_0 = \arcsin\left(\frac{n}{n_0}\cos\frac{\tau}{2}\right) + \frac{\tau-\pi}{2}. \tag{8}$$

The non-diffraction range can be written as

$$Z = \omega_0/\tan\alpha_0. \tag{9}$$

The THz beam is focused onto the SUT through the designed quasi-optical system, as illustrated in Fig. 3. The THz beam is radiated by a transmitting antenna (Tx, rectangular horn antenna, with a 10 dB beam width of 16°) with linear polarization at 150–220 GHz. Subsequently, the THz beam is collimated using a polytetrafluoroethylene lens (L1, $f = 100$ mm) and then directed towards the axicon or L2 after passing through a beam splitter (BS). This yields either a Bessel beam or Gaussian beam, both of which are then focused onto the SUT. The resulting echo signal, containing target information, is captured by a receiving antenna (Rx, rectangular horn antenna, with a 10 dB beam width of 16°) via an off-axis parabolic mirror (PM).

For quasi-optical imaging systems, it is crucial to ensure that all quasi-optical components are precisely aligned along a single axis. If L1 is not properly aligned with the BS, it can lead to misalignment in subsequent optical paths, directly affecting the quality of the system's PSF. To enhance the stability of the quasi-optical system, we employed a cage-like structure during the experimental process, as illustrated in Fig. 3. To further improve system robustness, we encapsulated the quasi-optical components and transceiver modules using 3D-printed structures made of rigid plastic material. This approach not only increased the convenience of testing operations, but also enhanced the

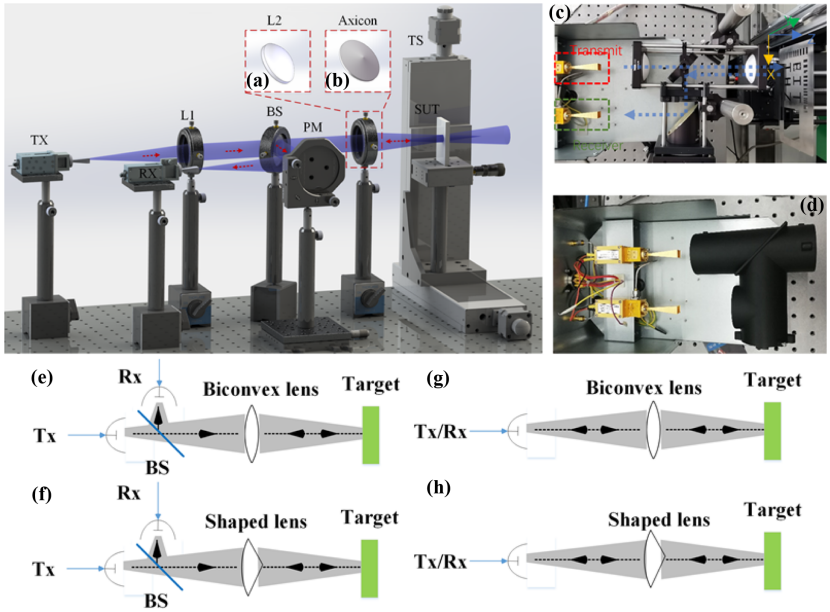

Fig. 3. Experimental setup of the THz FMCW radar imaging. Tx/Rx,150–220 GHz; BS, beam splitter; PM, off-axis parabolic mirror; TS, translation stage; SUT, sample under test. (a) Lens (L2, $f = 100$ mm) used to generate the Gaussian beam, (b) axicon used to generate the Bessel beam, (c) quasi-optical system based on a cage-like structure, and (d) quasi-optical system based on 3D-printed encapsulation. (e) and (f) are the separated transmit-receive configurations; (g) and (h) are, the integrated transmit-receive configurations.

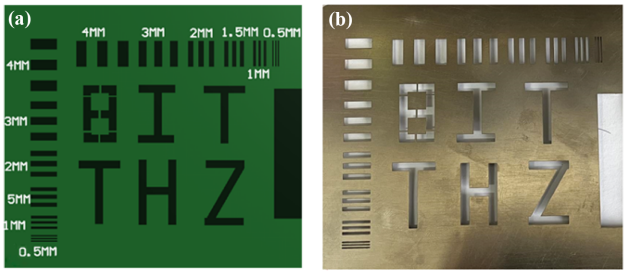

Fig. 4. Experimental test sample. (a) Design drawing of the resolution test target and (b) optical photo of the resolution test target.

overall system's robustness, as depicted in Fig. 3(d). For a separated transmit-receive system, we can simplify the system by reducing the physical separation between components and even potentially minimizing the number of quasi-optical devices, resulting in a more streamlined system, as depicted in Figs. 3(e) and 3(f), where the biconvex lens serves the purpose of both L1 and L2, while the shaped lens functions as both L1 and the axicon. As depicted in Figs. 3(g) and 3(h), the system structure can be further simplified by adopting an integrated transmit-receive module. However, this approach may result in a reduction in the system's dynamic range.

The resolution target employed for testing is displayed in Fig. 4(a), with a physical dimension of each pair being 4, 3, 2, 1, 1.5, and 0.5 mm. Additionally, the spacing between both the pairs and the width of the BIT THZ letter is 3 mm. Our system employs a diffractive element with a base angle of 15° to generate the zero-order Bessel beam, which has a theoretical FWHM of 3.7 mm that is equivalent to the FWHM of the focused Gaussian beam. The Gaussian beam has a calculated depth of field of 50 mm, whereas the non-diffraction range of the Bessel beam extends to 90 mm, significantly expending the focus depth of the Gaussian beam. During the imaging process, the scanning interval in the XY direction is set to 1 mm to satisfy the spatial sampling rate requirements. For the Gaussian beam imaging experiment, we define the target position where the echo signal intensity is constant as $z = 0$ mm and place the resolution test target at different positions within the Gaussian beam depth of field for testing. For the Bessel beam imaging experiment, the front surface of the axicon is defined as a position of $z = 0$ mm, and then imaging testing is performed away from the axicon.

Figures 5(a)–5(e) show the imaging results under the Gaussian beam at $z = -20$ mm, $z = -10$ mm, $z = 0$ mm, $z = 10$ mm, and $z = 20$ mm, respectively. It can be seen that the imaging results are clearest at $z = 0$ mm. However, the image begins to blur when $z > 10$ mm or $z < -10$ mm, as the resolution test target moves away from the focus position. The imaging result deteriorates as the Gaussian PSF increases, with a depth of field less than 20 mm. Figures 6(a)–6(f) show the imaging results under the Bessel beam at $z = 20$ mm, $z = 30$ mm, $z = 40$ mm, $z = 50$ mm, $z = 60$ mm, and $z = 70$ mm, respectively. It can be seen that, within 20–60 mm, the 3 mm line pair is still clearly visible, further verifying the large depth of field advantage of the Bessel beam in the THZ FMCW imaging system. When z is greater than 60 mm, the imaging result deteriorates as the Bessel PSF deteriorates. It is worth noting that the color values of the images represent the intensity information of the echoes, and all the measured result images are given in units of dB. Our previous work focused on the depth of field extension and resolution improvement in the range profile [42]. In contrast, this paper focuses on depth of field extension and resolution improvement in the lateral. Furthermore, different parameters of the quasi-optical devices are employed, resulting in varying levels of depth of field improvement.

C. Image Restoration Algorithm

For THz real-aperture imaging system, the lateral resolution is mainly limited by the PSF (the premise is that the spatial sampling interval should meet Nyquist sampling), and the imaging can be regarded as the convolution process between the THz beam and the target function. The 3D imaging degradation model based on the THz Bessel beam can be described as

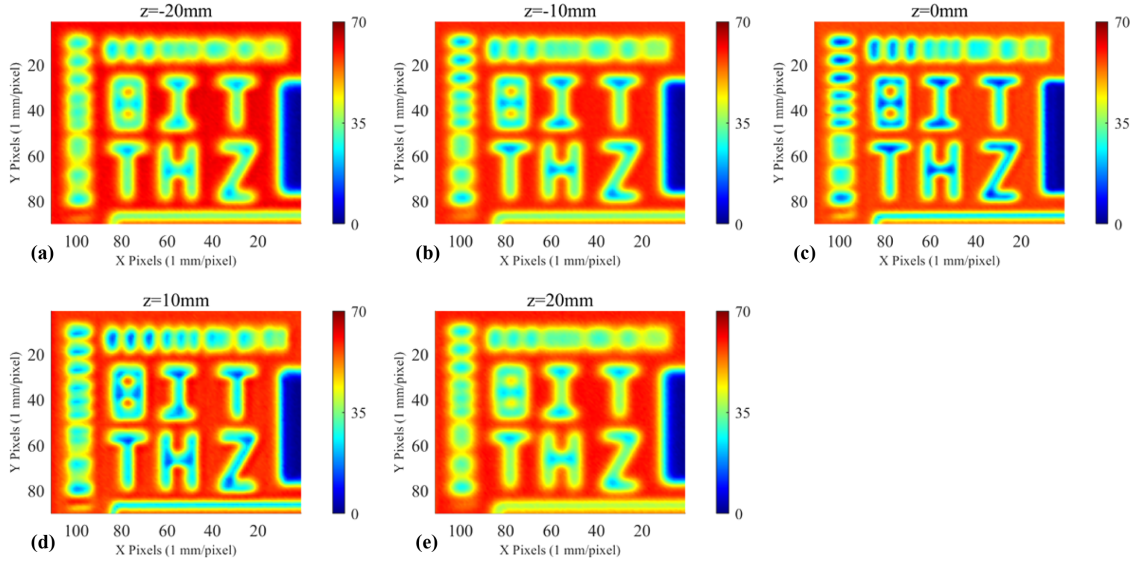

Fig. 5. Resolution test target imaging results at different z positions of the Gaussian beam. (a) $z = -25$ mm, (b) $z = -15$ mm, (c) $z = 0$ mm, (d) $z = 10$ mm, and (e) $z = 25$ mm.

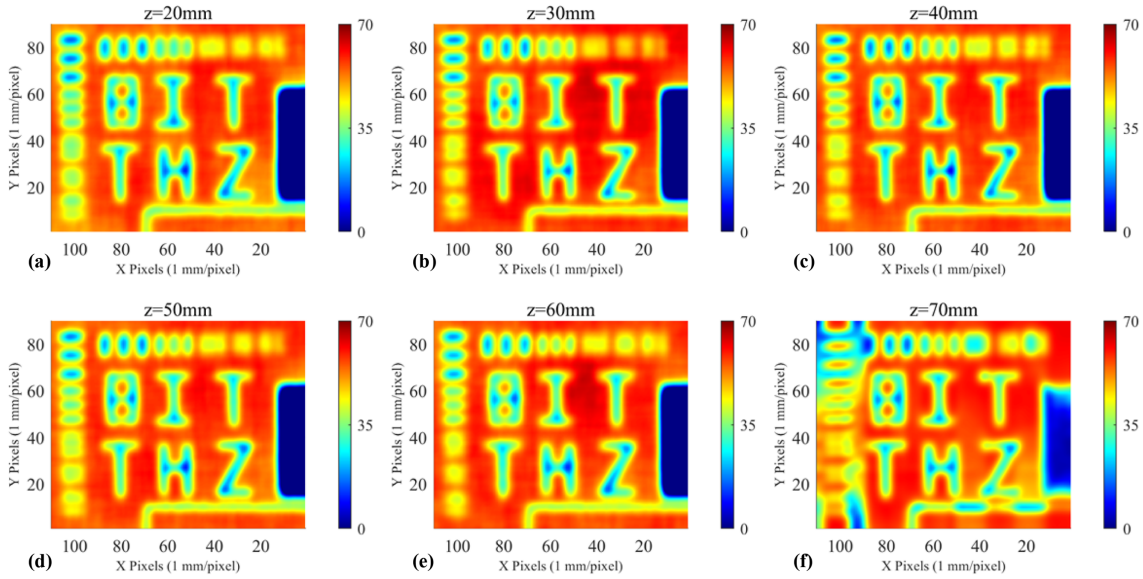

Fig. 6. Resolution test target imaging results at different z positions of the Bessel beam. (a) $z = 20$ mm, (b) $z = 30$ mm, (c) $z = 40$ mm, (d) $z = 50$ mm, (e) $z = 60$ mm, and (f) $z = 70$ mm.

$$lr(x, y, z) = hr(x, y, z) \otimes \mathrm{psf}(x, y, z) + n, \tag{10}$$

where $lr(x, y, z)$ is the resulting blurred image, $hr(x, y, z)$ is the ground truth of target, $\mathrm{psf}(x, y, z)$ is the quasi-optical system PSF, n is the noise introduced by the hardware, and $\otimes$ is the 3D convolution operation. Our goal is to recover $hr(x, y, z)$ from the degenerate model.

Similar to the traditional Gaussian beam imaging system, the blurred image obtained by the Bessel beam imaging system can be regarded as the convolution of the target function and the Bessel function, so that the lateral resolution can be further improved by deconvolution [24]. However, the existing image restoration methods mostly use the ideal PSF to deconvolute. In fact, due to the diffraction and refraction effects of the THz wave, the beam undergoes deformation during its transmission through complex multi-layer mediums and the introduction of the Bessel beam, playing a critical role in circumventing such issues. In addition, the processing and debugging errors of quasi-optical devices will further affect the actual PSF, causing a mismatch between the actual and the ideal PSF, and reduces the quality of the restored image. Conversely, it is more advantageous and universal to estimate the PSF from the information of the image.

The existing THz FMCW radar mainly adopts the electronic frequency multiplication method, and its imaging quality directly depends on the phase noise of the frequency sweep source. In this paper, our system uses the PLL to generate an FMCW signal, and the phase noise in the whole frequency band is better than −79 dBc/Hz at 1 kHz. In addition, nonlinearities within the IF signal are eliminated using nonlinearity calibration algorithm [43], thereby significantly improving the signal-to-noise ratio of the range profile. Meanwhile, it minimizes the impact of image noise on the accurate estimation of the PSF by deconvolution algorithms.

For the imaging target, the local gradient of the ground truth is larger than that of the blurred image [44], and the local gradient operator $L(hr(x))$ of the image block is introduced:

$$L(hr(x)) = \max_{y \in P(x)} (\max(\nabla hr(y))), \tag{11}$$

where x, y is the position of the pixels in the THz image, ∇ is a 2D gradient operator, $P(x)$ is a local image block centered on x, and hr is the ground truth.

The simplified formula (11) can be obtained by introducing the sparse matrix $\boldsymbol{G}$ [45]:

$$L(hr) = \boldsymbol{G}hr. \tag{12}$$

Scaling and deriving the formula (12) and introducing the L1 norm, the gradient of the ground truth and the blurred image has the following relationship:

$$\|2 - L(lr)\|_1 \geq \|2 - L(hr)\|_1. \tag{13}$$

Then we can construct the deblurring framework based on the image local gradient:

$$\min_{hr,\mathrm{psf}} \|hr \otimes \mathrm{psf} - lr\|_2 + \beta\|2 - L(hr)\|_1 + \gamma\|\nabla hr\|_0 + \tau\|\mathrm{psf}\|_2, \tag{14}$$

where β, γ, and τ are the coefficients of each regularization term.

We further decompose the deblurring framework into two subproblems, solving psf and hr:

$$\begin{cases} \mathrm{psf} = \min\limits_{\mathrm{psf}} \|\nabla hr \otimes \mathrm{psf} - lr\|^2 + \tau\|\mathrm{psf}\|^2 \\ hr = \min\limits_{hr} \|hr \otimes \mathrm{psf} - lr\|^2 + \beta\|g\|_1 + \gamma\|\nabla hr - f\|_0 \end{cases}. \tag{15}$$

The hr of formula (15) can be estimated by the semi-quadratic splitting method [46]. By introducing substitution variables $m = 2 - L(hr)$, $n = \nabla hr$, hr can be rewritten as

$$hr = \min_{hr,m,n} \left\| hr \otimes \mathrm{psf} - lr \right\|^2 + \beta \|m\|_1 + \gamma \|n\|_0 + \alpha_1 \|2 - L(hr) - m\| + \alpha_2 \|\nabla hr - n\|, \tag{16}$$

where α_1, α_2 are the penalty parameters, and Eq. (16) can be written in vector form by given α_1, α_2 and sparse matrix $\boldsymbol{G}$:

$$\min_{hr} \|\boldsymbol{k}hr - lr\|^2 + \alpha_1 \|2 - \boldsymbol{G}hr - \boldsymbol{m}\|^2 + \alpha_2 \|\nabla hr - \boldsymbol{n}\|^2. \tag{17}$$

In order to reduce the amount of calculation, we introduce auxiliary variable $\boldsymbol{p}$ to replace hr:

$$\begin{cases} \min\limits_{hr} \|\boldsymbol{k}hr - lr\|^2 + \alpha_2 \|\nabla hr - \boldsymbol{n}\|^2 + \alpha_3 \|hr - \boldsymbol{p}\|^2 \\ \min\limits_{\boldsymbol{p}} \alpha_1 \|2 - \boldsymbol{G}\boldsymbol{p} - \boldsymbol{m}\|^2 + \alpha_3 \|hr - \boldsymbol{p}\|^2 \end{cases}, \tag{18}$$

where α_3 is the introduced penalty parameter.

We can solve formula (18) by various FFT [47] operations and get the optimal solution of hr and $\boldsymbol{p}$:

$$hr = \mathcal{F}^{-1}\left(\frac{\overline{\mathcal{F}(\mathbf{psf})}\mathcal{F}(\boldsymbol{l}r) + \alpha_2 \overline{\mathcal{F}(\nabla)}\mathcal{F}(\boldsymbol{n}) + \alpha_3 \mathcal{F}(\boldsymbol{p})}{\overline{\mathcal{F}(\mathbf{psf})}\mathcal{F}(\mathbf{psf}) + \alpha_2 \overline{\mathcal{F}(\nabla)}\mathcal{F}(\nabla) + \alpha_3} \right), \tag{19}$$

$$\boldsymbol{p} = \frac{\alpha_1 \boldsymbol{G}^T (2 - \boldsymbol{m}) + \alpha_3 hr}{\alpha_1 \boldsymbol{G}^T \boldsymbol{G} + \alpha_3}, \tag{20}$$

where $\mathcal{F}(\cdot)$ is the FFT operation, $\mathcal{F}^1(\cdot)$ is the inverse FFT, and $\bar{\cdot}$ is the conjugate operation.

We iteratively update $\boldsymbol{m}$ and $\boldsymbol{n}$ through the following two subequations:

$$\begin{cases} \min\limits_{\boldsymbol{m}} \beta \|\boldsymbol{m}\|_1 + \alpha_1 \|2 - \boldsymbol{G}hr - \boldsymbol{m}\|^2 \\ \min\limits_{\boldsymbol{n}} \rho \|\boldsymbol{n}\|_0 + \alpha_2 \|\nabla hr - \boldsymbol{n}\|^2 \end{cases}. \tag{21}$$

Here we solve for $\boldsymbol{m}$ and $\boldsymbol{n}$ with a pixel-by-pixel optimization algorithm [46]:

$$\boldsymbol{m} = \mathrm{sign}(2 - \boldsymbol{G}hr) \cdot \max(|2 - \boldsymbol{G}hr|, 0), \tag{22}$$

$$\boldsymbol{n} = \nabla hr \left(|\nabla hr|^2 \geq \frac{1}{\alpha_2} \right), \quad 0 \text{ (otherwise)}. \tag{23}$$

In addition, the least squares method is used to solve the convolution kernel part [48], and the PSF in formula (15) can be rewritten as

$$\mathrm{psf} = \min_{\mathrm{psf}} \left\| \nabla hr \otimes \mathrm{psf} - \nabla lr \right\|^2 + \tau \left\| \mathrm{psf} \right\|^2. \tag{24}$$

We can solve it with the FFT directly:

$$\mathrm{psf} = \mathcal{F}^{-1}\left(\frac{\overline{\mathcal{F}(\nabla hr)}\mathcal{F}(\nabla lr)}{\overline{\mathcal{F}(\nabla hr)}\mathcal{F}(\nabla hr) + \tau} \right). \tag{25}$$

The process flow of the THz image restoration algorithm is shown in Fig. 7. It is worth noting that our paper uses the prior information of the convolution kernel (we use the ideal PSF as input) to accelerate the convergence of the algorithm. The restoration takes 18 s with a desktop computer (i7-12700H, 16 GB RAM). Additionally, for different imaging objects, fine adjustments of the algorithm's initial parameters are required to achieve better restoration results, which may lead to a slight reduction in computational efficiency.

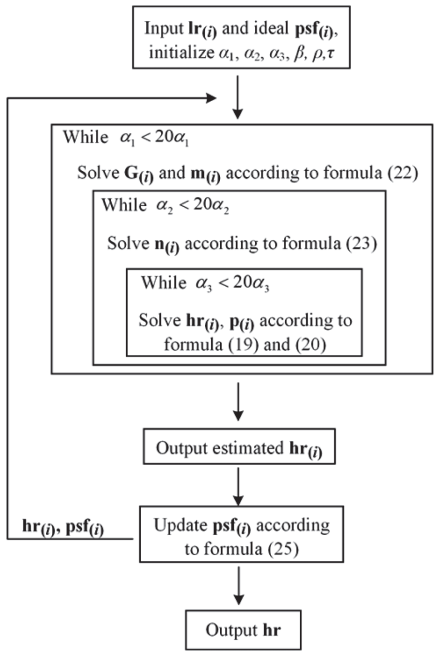

Fig. 7. Flow chart of the proposed THz image restoration algorithm.

3. RESULTS ANALYSIS

The synthetic resolution target is displayed in Fig. 8(g), where the numbers represent line pairs ranging from 1 to 10 mm, and the width of each line pair is consistent with the interval size. The noise level is 0.003, and the size of the 3 dB convolution kernel is set to 5 mm. It is apparent from the results that bicubic interpolation merely increases the number of pixels without significantly enhancing the lateral resolution. It is worth noting that other methods perform the bicubic interpolation to ensure that the number of image pixels is consistent. As depicted in Figs. 8(c) and 8(d), the Lucy—Richardson and Wiener methods improve the resolution to a certain degree, albeit accompanied by amplified noise. Our proposed method exploits precise PSF estimation and hence generates an improved restoration image, revealing clearly visible 3 mm line pairs. Table 1 is the peak signal-to-noise ratio (PSNR) and structural similarity (SSIM) comparison results of various methods for the synthetic resolution test target.

We select the imaging result of the Bessel beam at $z = 50$ mm as the blurred image input, and the image restoration results of various methods as shown in Fig. 9. Although the Wiener method has been improved to a certain extent, the 3 mm line pair is slightly clearer than the degraded synthetic resolution target, it is accompanied by the amplification of noise, which deteriorates the image quality. The Lucy—Richardson method has a more obvious improvement effect on 3 mm line pairs, but the noise deterioration is more serious. Although the blind-deconvolution method has a better effect than the previous two

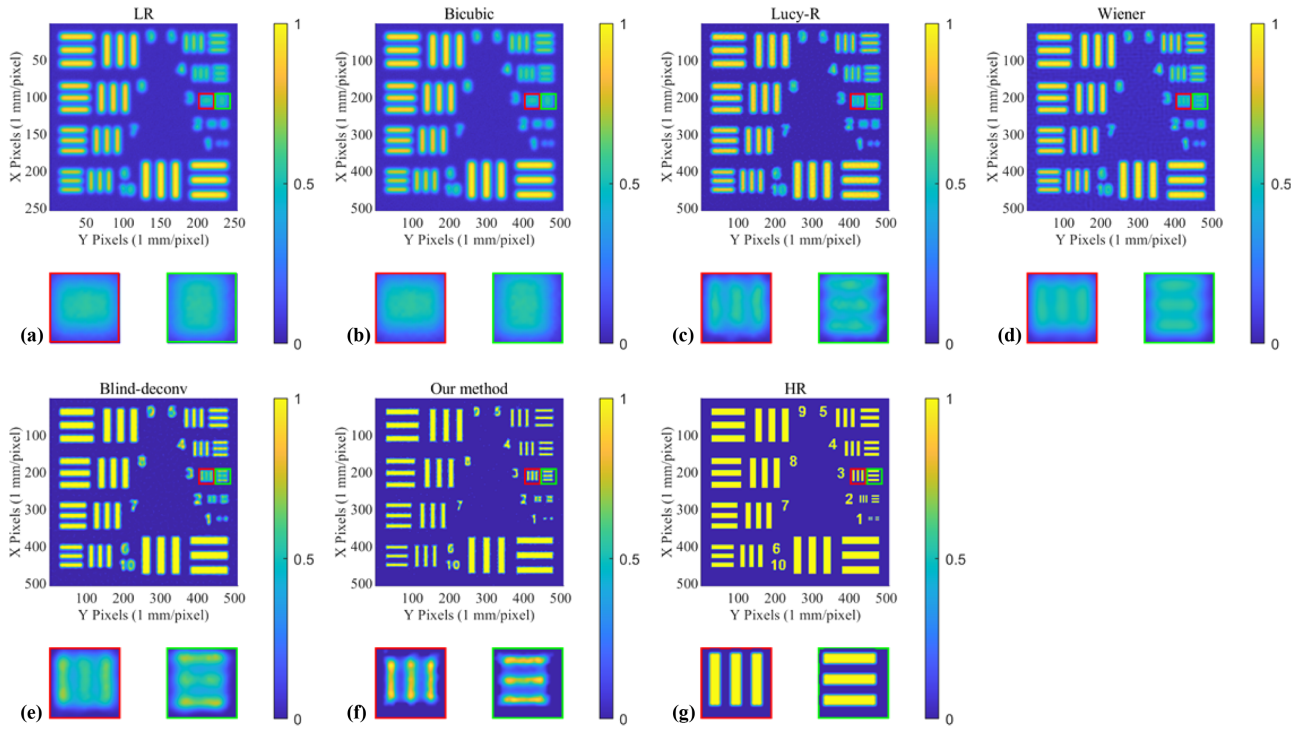

Fig. 8. Comparison of different methods on the synthetic resolution test target. (a) Degraded synthetic resolution target (low resolution, LR); (b) bicubic interpolation; (c) Lucy–Richardson deconvolution; (d) Wiener deconvolution; (e) normalized sparsity measurement blind-deconvolution; (f) our method; and (g) synthetic resolution target (high resolution, HR).

Table 1. Comparison Results of Different Methods for the Synthetic Image

Restoration Level	PSNR (dB)	SSIM
Bicubic	19.8625	0.6380
Lucy–Richardson	21.4332	0.6920
Wiener	20.8374	0.7012
Blind-deconv	23.7397	0.7826
Our Method	**24.6405**	**0.8304**

methods and has a good noise control ability, the overall image is somewhat distorted. Our method benefits from the prior constraints on the image and the accurate estimation of the PSF, making the 2 mm line pairs visible while maintaining a low noise level and obtaining the best image restoration effect.

In addition, benefiting from the large depth of field advantage of the Bessel beam, we further apply it to the field of NDT of semiconductor devices. We choose the arm emulator for programming and debugging programs in the chip design as the test target. Figure 10(a) is the optical photo of the arm emulator, and Fig. 10(b) is the internal circuit structure, which includes tiny components such as crystal oscillators and chips. Figures 10(c) and 10(d) are the measured dimensions of the crystal oscillator with the width and length as 3 and 9.2 mm, respectively. We use a 2D electric translation stage to scan the arm simulator in the XY direction (the scanning interval is 1 mm) and obtain its 3D imaging results.

The segment of the 3D tomographic data that contains crystal oscillator information is chosen, and the proposed algorithm along with other techniques are employed for deconvolution. As shown in Fig. 11(a), it is the original imaging result at $z = 40$ mm (taking the front surface of the arm emulator as $z = 0$ mm). Due to the degradation of the THz Bessel beam, the characteristics and contours of the crystal oscillator area on the circuit board are blurred. Following bicubic interpolation, as demonstrated in Fig. 11(b), image smoothness improves as the pixel count increases, but the effective information stays the same. As non-blind methods, the Lucy—Richardson and Wiener methods usually deconvolute with the ideal PSF, as shown in Figs. 11(c) and 11(e). Although the overall visual effect of the restored image is more "clear," the effective information of the circuit board becomes blurred, and the crystal oscillator area is severely distorted. It is the mismatch between the actual and ideal PSF that causes the loss of image fidelity, so the real size of the crystal oscillator cannot be restored. Compared with the first two methods, the restored crystal shape is close to the real size in Fig. 11(d). However, it still does not match and indirectly explains the limitation of the PSF accuracy estimated by blind-deconvolution. Figure 11(f) shows the restoration results of the proposed algorithm. It can be seen that the lateral resolution has been greatly improved. The length and width of the restored crystal oscillator are 2.9 and 8.9 mm, respectively, which are consistent with the actual crystal shape. Moreover, the restored image has good fidelity, which further confirms the advantages of the proposed image restoration algorithm in the field of NDT.

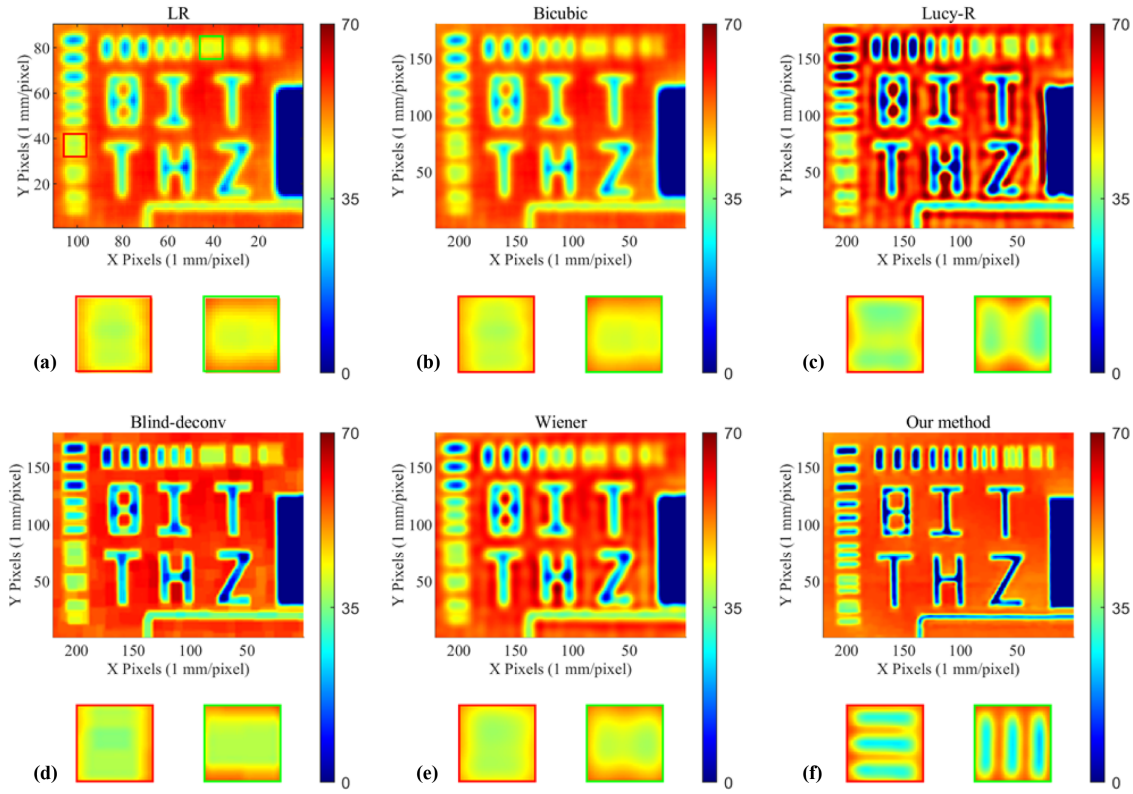

Fig. 9. Comparison of the results when the resolution test target is located at $z = 50$ mm of the Bessel beam. (a) Measured resolution board image (b) bicubic interpolation, (c) Lucy–Richardson deconvolution, (d) normalized sparsity measurement blind-deconvolution, (e) Wiener deconvolution, and (f) our method.

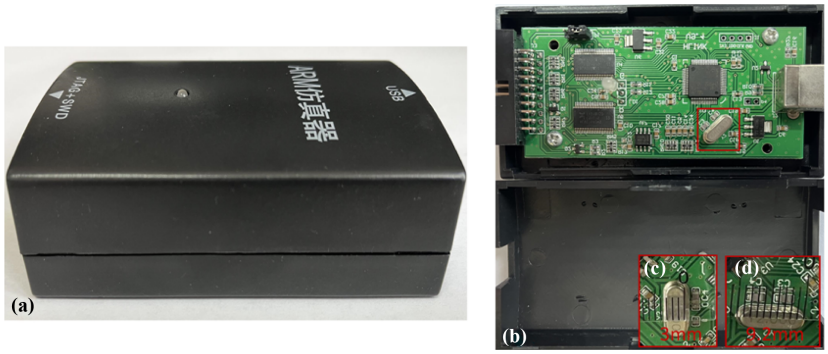

Fig. 10. Tested semiconductor devices. (a) Arm emulator and (b) its inner structure. (c) and (d) are the amplified part of the red box area in (b), and the length and width of the crystal oscillator are 3 and 9.2 mm, respectively.

4. CONCLUSION

In this paper, a large depth of field THz FMCW radar system is developed. Benefiting from the large depth of field and self-restoration of the THz Bessel beam, the space invariance of the PSF during transmission is effectively guaranteed. The results of the resolution test target reflect its advantage in the THz FMCW real-aperture radar system, which is more suitable for imaging detection of multi-layer complex media, and further reduces the pressure of the deconvolution algorithm on complex PSF estimation. Moreover, an image restoration algorithm using the image gradient information and the convolution kernel prior is proposed. Compared with the traditional algorithm, our algorithm improves the image under-restoration or over-restoration problem caused by the mismatch between the ideal and actual PSF, getting better image fidelity. The proposed quasi-optical system and algorithm can be extended to THz real-aperture imaging systems, which have great application potential in imaging fields such as NDT and standoff personnel screening.

Funding. National Natural Science Foundation of China (61527805, 61731001).

Disclosures. The authors declare no conflicts of interest.

Data availability. Data underlying the results presented in this paper are not publicly available at this time but may be obtained from the authors upon reasonable request.

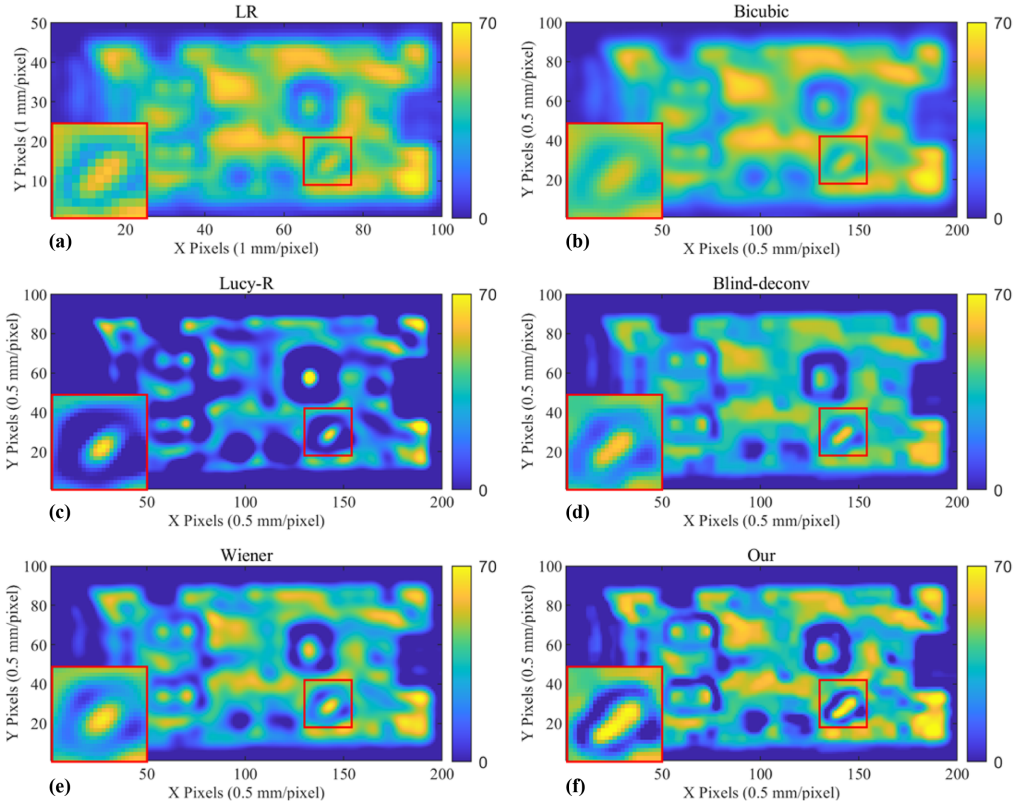

Fig. 11. Bessel beam imaging results of the arm emulator by different image methods. (a) Measured arm emulator image, (b) bicubic interpolation, (c) Lucy–Richardson deconvolution, (d) normalized sparsity measurement blind-deconvolution, (e) Wiener deconvolution, and (f) our method.

REFERENCES

1. G. Rubio-Cidre, A. Badolato, L. Ubeda-Medina, J. Grajal, B. Mencia-Oliva, and B. P. Dorta-Naranjo, "DDS-based signal-generation architecture comparison for an imaging radar at 300 GHz," IEEE Trans. Instrum. Meas. **64**, 3085–3098 (2015).
2. K. B. Cooper, R. J. Dengler, N. Llombart, B. Thomas, and P. H. Siegel, "THz imaging radar for standoff personnel screening," IEEE Trans. Terahertz Sci. Technol. **1**, 169–182 (2011).
3. H. Gao, C. Li, S. Zheng, S. Wu, and G. Fang, "Implementation of the phase shift migration in MIMO-sidelooking imaging at terahertz band," IEEE Sens. J. **19**, 9384–9393 (2019).
4. I. F. Akyildiz, J. M. Jornet, and H. Chong, "Terahertz band: next frontier for wireless communications," Phys. Commun. **12**, 16–32 (2014).
5. S. M. Kim, F. Hatami, J. S. Harris, A. W. Kurian, J. Ford, D. King, G. Scalari, M. Giovannini, N. Hoyler, and J. Faist, "Biomedical terahertz imaging with a quantum cascade laser," Appl. Phys. Lett. **88**, 153903 (2006).
6. H. Liu, Z. Zhang, X. Zhang, Y. Yang, Z. Zhang, X. Liu, F. Wang, Y. Han, and C. Zhang, "Dimensionality reduction for identification of hepatic tumor samples based on terahertz time-domain spectroscopy," IEEE Trans. Terahertz Sci. Technol. **8**, 271–277 (2018).
7. G. Ren, L. Zhou, L. Chen, L. Liu, J. Zhang, H. Zhao, and J. Han, "Application of terahertz spectroscopy on monitoring crystallization and isomerization of azobenzene," Opt. Express **29**, 14894–14904 (2021).
8. H. Huang, P. Qiu, S. Panezai, S. Hao, D. Zhang, Y. Yang, Y. Ma, H. Gao, L. Gao, Z. Zhang, and Z. Zheng, "Continuous-wave terahertz high-resolution imaging via synthetic hologram extrapolation method using pyroelectric detector," Opt. Laser Technol. **120**, 105683 (2019).
9. H. Cheng, H. Huang, M. Yang, M. Yang, H. Yan, S. Panezai, Z. Zheng, Z. Zhang, and Z. Zhang, "Characterization of the remediation of chromium ion contamination with bentonite by terahertz time-domain spectroscopy," Sci. Rep. **12**, 11149 (2022).
10. X. Feng, Q. Wang, Y. Lu, Q. Xu, X. Zhang, L. Niu, X. Chen, Q. Li, J. Han, and W. Zhang, "Direct emission of broadband terahertz cylindrical vector Bessel beam," Appl. Phys. Lett. **119**, 221110–221116 (2021).
11. P. Zhang, T. Cai, Q. Zhou, G. She, W. Liang, Y. Deng, T. Ning, W. Shi, L. Zhang, and C. Zhang, "Ultrahigh modulation enhancement in all-optical Si-based THz modulators integrated with gold nanobipyramids," Nano Lett. **22**, 1541–1548 (2022).
12. J. Dong, J. B. Jackson, M. Melis, D. Giovanacci, G. C. Walker, A. Locquet, J. W. Bowen, and D. S. Citrin, "Terahertz frequency-wavelet domain deconvolution for stratigraphic and subsurface investigation of art painting," Opt. Express **24**, 26972–26985 (2016).
13. C. Dandolo, J. P. Guillet, M. Xue, F. Fauquet, and P. Mounaix, "Terahertz frequency modulated continuous wave imaging advanced data processing for art painting analysis," Opt. Express **26**, 5358–5367 (2018).
14. F. Ellrich, M. Bauer, N. Schreiner, A. Keil, and D. Molter, "Terahertz quality inspection for automotive and aviation industries," J. Infrared Millim. Terahertz Waves **41**, 470–489 (2020).
15. M. Bauer, R. Hussung, C. Matheis, H. Reichert, P. Weichenberger, J. Beck, U. Matuschczyk, J. Jonuscheit, and F. Friederich, "Fast FMCW terahertz imaging for in-process defect detection in press sleeves for the paper industry and image evaluation with a machine learning approach," Sensors **21**, 6569–6587 (2021).
16. W. Hu, Z. Xu, Z. Han, H. Jiang, Y. Liu, Y. Lu, and L. P. Ligthart, "Ultra-wideband signal generation and fusion algorithm for high-resolution terahertz FMCW radar imaging," Opt. Express **30**, 9814–9822 (2022).
17. E. Cristofani, F. Friederich, S. Wohnsiedler, C. Matheis, and R. Beigang, "Non-destructive testing potential evaluation of a THz frequency-modulated continuous-wave imager for composite materials inspection," Opt. Eng. **53**, 031211 (2014).
18. D. C. Popescu and A. D. Hellicar, "Point spread function estimation for a terahertz imaging system," EURASIP J. Adv. Signal Process. **2010**, 575817 (2010).

19. K. Ahi, "Mathematical modeling of THz point spread function and simulation of THz imaging systems," IEEE Trans. Terahertz Sci. Technol. **7**, 747–754 (2017).
20. J. Durnin, "Exact solutions for nondiffracting beams. I. The scalar theory," J. Opt. Soc. Am. A **4**, 651–654 (1987).
21. G. Ok, S. W. Choi, K. H. Park, and H. S. Chun, "Foreign object detection by sub-terahertz quasi-bessel beam imaging," Sensors **13**, 71–85 (2012).
22. A. Bitman, I. Moshe, and Z. Zalevsky, "Improving depth-of field in broadband THz beams using nondiffractive Bessel beams," Opt. Lett. **37**, 4164–4166 (2012).
23. A. Bitman, S. Goldring, I. Moshe, and Z. Zalevsky, "Computed tomography using broadband Bessel THz beams and phase contrast," Opt. Lett. **39**, 1925–1928 (2014).
24. L. Minkeviius, D. Jokubauskis, I. Kaalynas, S. Orlov, A. Urbas, and G. Valušis, "Bessel terahertz imaging with enhanced contrast realized by silicon multi-phase diffractive optics," Opt. Express **27**, 36358–36367 (2019).
25. G. B. Wu, K. F. Chan, and C. H. Chan, "3-D printed terahertz lens to generate higher order Bessel beams carrying OAM," IEEE Trans. Antennas Propag. **69**, 3399–3408 (2021).
26. L. Niu, K. Wang, Y. Yang, Q. Wu, X. Ye, Z. Yang, J. Liu, and H. Yu, "Diffractive elements for zero-order Bessel beam generation with application in the terahertz reflection imaging," IEEE Photonics J. **11**, 1–12 (2019).
27. X. Wei, C. Liu, L. Niu, Z. Zhang, K. Wang, Z. Yang, and J. Liu, "Generation of arbitrary order Bessel beams via 3D printed axicons at the terahertz frequency range," Appl. Opt. **54**, 10641–10649 (2015).
28. M. S. Kulya, V. A. Semenova, V. G. Bespalov, and N. V. Petrov, "On terahertz pulsed broadband Gauss-Bessel beam free-space propagation," Sci. Rep. **8**, 1390–1400 (2018).
29. Z. Wu, X. Wang, W. Sun, S. Feng, P. Han, J. Ye, Y. Yu, and Y. Zhang, "Vectorial diffraction properties of THz vortex Bessel beams," Opt. Express **26**, 1506–1520 (2018).
30. Z. Zhang, H. Zhang, and K. Wang, "Diffraction-free THz sheet and its application on THz imaging system," IEEE Trans. Terahertz Sci. Technol. **9**, 471–475 (2019).
31. A. Siemion, "The magic of optics—an overview of recent advanced terahertz diffractive optical elements," Sensors **21**, 100–121 (2021).
32. S. H. Ding, Q. Li, R. Yao, and Q. Wang, "High-resolution terahertz reflective imaging and image restoration," Appl. Opt. **49**, 6834–6839 (2010).
33. L. M. Xu, W. H. Fan, and J. Liu, "High-resolution reconstruction for terahertz imaging," Appl. Opt. **53**, 7891–7897 (2014).
34. T. M. Wong, M. Kahl, P. Haring Bolívar, and A. Kolb, "Computational image enhancement for frequency modulated continuous wave (FMCW) THz image," J. Infrared Millim. Terahertz Waves **40**, 775–800 (2019).
35. D. Krishnan, T. Tay, and R. Fergus, "Blind deconvolution using a normalized sparsity measure," in *Proceedings, IEEE Conference on Computer Vision and Pattern Recognition* (2011), pp. 233–240.
36. Y. Wang, F. Qi, and J. Wang, "Terahertz image super-resolution based on a complex convolutional neural network," Opt. Lett. **46**, 3123–3126 (2021).
37. Y. Wang, F. Qi, and J. Wang, "Complex "zero-shot" super-resolution reconstruction algorithm for THz imaging," Appl. Opt. **61**, 5831–5837 (2022).
38. X. Yang, D. Zhang, Z. Wang, Y. Zhang, J. Wu, B. Wu, and X. Wu, "Super-resolution reconstruction of terahertz images based on a deep-learning network with a residual channel attention mechanism," Appl. Opt. **61**, 3363–3370 (2022).
39. Q. Mao, Y. Zhu, C. Lv, Y. Lu, X. Yan, S. Yan, and J. Liu, "Convolutional neural network model based on terahertz imaging for integrated circuit defect detections," Opt. Express **28**, 5000–5012 (2020).
40. Z. Long, T. Wang, C. You, Z. Yang, K. Wang, and J. Liu, "Terahertz image super-resolution based on a deep convolutional neural network," Appl. Opt. **58**, 2731–2735 (2019).
41. Y. Li, W. Hu, X. Zhang, Z. Xu, J. Ni, and L. P. Ligthart, "Adaptive terahertz image super-resolution with adjustable convolutional neural network," Opt. Express **28**, 22200–22217 (2020).
42. W. Hu, Z. Xu, H. Jiang, Y. Liu, Z. Yao, K. Zhang, and L. P. Ligthart, "High range resolution wideband terahertz FMCW radar with a large depth of field," Appl. Opt. **61**, 7189–7196 (2022).
43. Y. Li, W. Hu, X. Zhang, Y. Zhao, J. Ni, and L. P. Ligthart, "A non-linear correction method for terahertz LFMCW radar," IEEE Access **8**, 102784–102794 (2020).
44. L. Chen, F. Fang, T. Wang, and G. Zhang, "Blind image deblurring with local maximum gradient prior," in *Proceedings, IEEE Conference on Computer Vision and Pattern Recognition* (2019), pp. 1742–1750.
45. J. Pan, D. Sun, H. Pfister, and M. H. Yang, "Blind image deblurring using dark channel prior," in *Proceedings, IEEE Conference on Computer Vision and Pattern Recognition* (2016), pp. 1628–1636.
46. L. Xu, S. Zheng, and J. Jia, "Unnatural L0 sparse representation for natural image deblurring," in *Proceedings, IEEE Conference on Computer Vision and Pattern Recognition* (2013), pp. 1107–1114.
47. Y. Yan, W. Ren, Y. Guo, R. Wang, and X. Cao, "Image deblurring via extreme channels prior," in *Proceedings, IEEE Conference on Computer Vision and Pattern Recognition* (2017), pp. 6978–6986.
48. A. Levin, Y. Weiss, F. Durand, and W. T. Freeman, "Efficient marginal likelihood optimization in blind deconvolution," in *Proceedings, IEEE Conference on Computer Vision and Pattern Recognition* (2011), pp. 2657–2664.